Bulletin of the Seismological Society of America, Vol. 107, No. 5, pp. 2183–2193, October 2017, doi: 10.1785/0120170077

Ⓔ

Fourth-Order Staggered-Grid Finite-Difference Seismic Wavefield Estimation Using a Discontinuous Mesh Interface (WEDMI)

by Shiying Nie, Yongfei Wang,* Kim B. Olsen, and Steven M. Day

Abstract In a realistic geological structure with a large contrast in seismic wavespeed between shallow and deep regions, simulation of seismic wave propagation using a spatially uniform grid can be computationally very demanding, due to overdiscretization of the high-speed material. Thus, numerical methods that allow for coarser discretization of the faster regions have the potential to be much more efficient. Discontinuous mesh (DM) methods, operating by exchanging wavefield information between media partitions discretized with two different grid spacings, provide a convenient way to improve such efficiency issues. Unfortunately, discontinuous staggered-grid finite-difference (FD) methods typically suffer from inherent stability problems, in particular in strongly heterogeneous media, arising from numerical noise generated at the overlap of the two regions with different grid spacing. We have developed a 3D fourth-order velocity-stress staggered-grid FD DM anelastic wave propagation method (AWP-DM) for seismic wavefield estimation using a discontinuous mesh interface (WEDMI) between fine and coarse meshes. Benchmarks in models with realistic 3D velocity variations and finite-fault sources across the grid interface show stable results for a number of timesteps, exceeding the need dictated by current high-frequency ground-motion simulations. In the case of a factor-of-three ratio between the coarse and fine grid sizes, this method is capable of producing a level of accuracy comparable to that from the uniform fine-grid scheme, using at least 7–8 grid points per minimum S wavelength inside the mesh overlap zone.

Electronic Supplement: Additional stability tests with wavefield estimation using a discontinuous mesh interface (WEDMI) and Lanczos 13p.

Introduction

Seismic wave propagation is a useful tool for modeling and imaging underground structures and earthquake sources. However, despite more widespread access to high-performance computing facilities in recent years, simulating high-frequency ground motions in a large-scale geologically realistic 3D structure is still an extremely computationally challenging problem. One of the most important reasons is the high contrast of seismic-wave velocities found in real earth structure, especially in sedimentary basins. Simulation of wave propagation that ignores the (often relatively) thin low-velocity regions produces inaccurate results, which can have important societal consequences (e.g., underprediction of seismic hazards). On the other hand, the low-velocity sediments are computationally extremely expensive to include, using a uniform grid size that is determined by the lowest velocity. The resulting oversampling for deeper region with higher velocity inevitably leads to a considerable increase of computational time and memory. For this reason, it is desirable to be able to use different discretizations in shallow and deep regions. Moczo (1989) and Pitarka (1999) developed finite-difference (FD) methods with grid spacing changing continuously over a distance separating a fine and coarse mesh, which are often less efficient and flexible to apply in realistic models as compared to discontinuous mesh (DM) methods. Jastram and Behle (1992) first designed a DM in their 2D acoustic FD method in which they enabled any integer ratio of coarse-to-fine grid size. Because these methods were proposed, different varieties of the DM approach, with the goal to more accurately and efficiently model realistic geological settings, have been proposed (e.g., Aoi and Fujiwara, 1999; Tessmer, 2000; Hayashi *et al.*,

*Also at Institute of Geophysics and Planetary Physics, Scripps Institution of Oceanography, University of California, San Diego, 9500 Gilman Drive, La Jolla, California 92093-0225.

2001; Wang *et al.*, 2001; Kang and Baag, 2004a,b; Kristek *et al.*, 2010; Zhang *et al.*, 2013).

However, several authors and users of the FD discontinuous grid implementations found that the methods suffer inherently from stability problems after a large number of timesteps (e.g., S. Aoi, written comm., 2016). We also note that the Lanczos filter that is already applied to several discontinuous algorithms (Kristek *et al.*, 2010; Zhang *et al.*, 2013; 2D Mimetic Operators from O. Rojas, unpublished report, 2014; see Data and Resources) has been proved to improve the stability of these schemes, but the performance of stability may vary in different numerical algorithms and material models (Zhang *et al.*, 2013; J. Kristek, written comm., 2016; 2D Mimetic Operators from O. Rojas, unpublished report, 2014; see Data and Resources).

In this article, we introduce a DM into a fourth-order staggered FD scheme to simulate anelastic wave propagation (AWP; Olsen, 1994; Olsen *et al.*, 1995). The continuous mesh implementation is now developed to be highly scalable on both CPU and GPU platforms (AWP-ODC [Olsen, Day and Cui]) used for large-scale simulations including TeraShake (Olsen *et al.*, 2006), TeraShake-2 (Olsen *et al.*, 2008), ShakeOut-D (Olsen *et al.*, 2009), and M8 (Cui *et al.*, 2010). AWP-ODC is also currently an important community modeling tool to better understand the dynamics of earthquakes and seismic hazards required to engineer safer buildings in southern California (Cui *et al.*, 2013). These simulations are being pushed to higher and higher maximum frequencies in efforts to meet the requirements of structural and geotechnical engineers for broadband estimates of input motion under diverse conditions on source and receiver, requiring stability up to a very large number of timesteps in a realistic 3D heterogeneous velocity model. Here, we introduce a new interface between the coarse and fine meshes (wavefield estimation using a discontinuous mesh interface [WEDMI]), and document the method for accuracy and stability in a series of benchmarks. These verification tests include a simple homogeneous model with a point source, a velocity model with a sharp contrast, and the Southern California Earthquake Center (SCEC) Community Velocity Model (CVM) v.4, for both point and extended sources.

Implementation of Discontinuous Mesh into AWP (AWP-DM)

AWP simulates 3D seismic wave propagation using the governing equations (velocity and stress system)

$$\frac{\partial v_i}{\partial t} = \frac{1}{\rho}\frac{\partial \sigma_{ij}}{\partial x_j}, \tag{1a}$$

$$\frac{\partial \sigma_{ij}}{\partial t} = \lambda\left(\frac{\partial v_i}{\partial x_i}\right)\delta_{ij} + \mu\left(\frac{\partial v_i}{\partial x_j} + \frac{\partial v_j}{\partial x_i}\right), \tag{1b}$$

in which $\mathbf{v}$ is the particle velocity vector, $\boldsymbol{\sigma}$ is the symmetric stress tensor, λ and μ are the Lamé coefficients, ρ is the density, δ_{ij} is the Kronecker delta, and i or $j = 1, 2, 3$ denoting the x, y, z directions. AWP solves equations (1a) and (1b) using an explicit staggered-grid FD scheme, which has second-order accuracy in time and fourth-order accuracy in space. Figure 1 shows the layout of the three velocity components and six stress components, indicating that the most straightforward way to implement a DM is to use a ratio of spatial discretization between coarse (H) and fine (h) grids (H/h) equal to an odd number. In this study, we only consider the case of $H/h = 3$ to demonstrate the basic scheme and the advantage of the DM. Figure 1 shows an example of updating v_x along the y direction to illustrate the DM algorithm in our FD method. Although the FD update for v_x requires the surrounding stress components at $\pm(1/2)h$ and $\pm(3/2)h$, the DM skips the nearest stress components and uses values at $\pm(3/2)h$ and at $\pm(9/2)h$ instead.

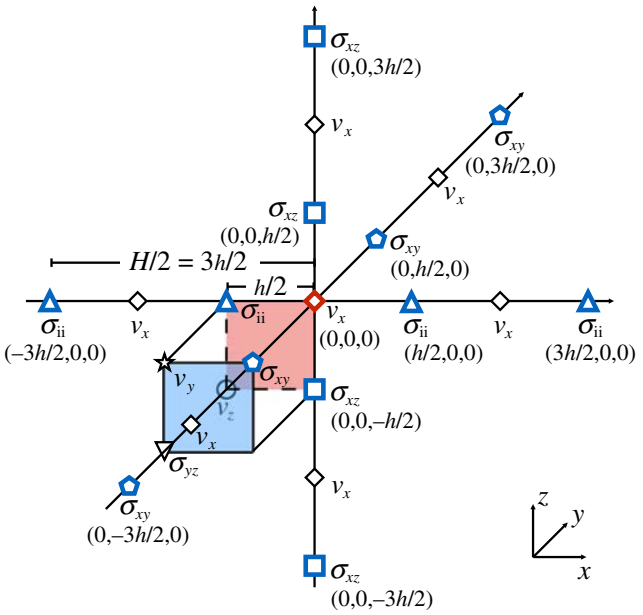

Figure 1. Layout of velocity and stress components for the fourth-order staggered-grid anelastic wave propagation (AWP) finite-difference (FD) method. Updating v_x at the pivot point requires σ_{ii} (σ_{xx}, σ_{yy}, and σ_{zz}) at $(-3h/2, 0, 0)$, $(-h/2, 0, 0)$, $(h/2, 0, 0)$, and $(3h/2, 0, 0)$, σ_{xy} at $(0, -3h/2, 0)$, $(0, -h/2, 0)$, $(0, h/2, 0)$, and $(0, -3h/2, 0)$, σ_{xz} at $(0, 0, -3h/2)$, $(0, 0, -h/2)$, $(0, 0, h/2)$, and $(0, 0, 3h/2)$. A discontinuous mesh (DM) method with a ratio of grid spacing (H/h) of three skips the nearest stress components at $(-h/2, 0, 0)$, $(h/2, 0, 0)$, $(0, -h/2, 0)$, $(0, h/2, 0)$, $(0, 0, -h/2)$, and $(0, 0, h/2)$ and uses values at $(-3h/2, 0, 0)$, $(3h/2, 0, 0)$, $(0, -3h/2, 0)$, $(0, 3h/2, 0)$, $(0, 0, -3h/2)$, and $(0, 0, 3h/2)$ to update v_x at $(0, 0, 0)$ instead. The two shaded patches belong to two parallel XZ planes containing different wavefield components described in detail in Figure 2 (right and left, respectively). The color version of this figure is available only in the electronic edition.

A critical part of the DM is the overlap zone at the grid interface between the (shallow) fine and (deep) coarse regions, across which the particle velocity and stress tensor are required to be exchanged to guarantee the continuity of the seismic wavefield. Both transmissions of wavefield information from the coarse to fine grid and from the fine to coarse

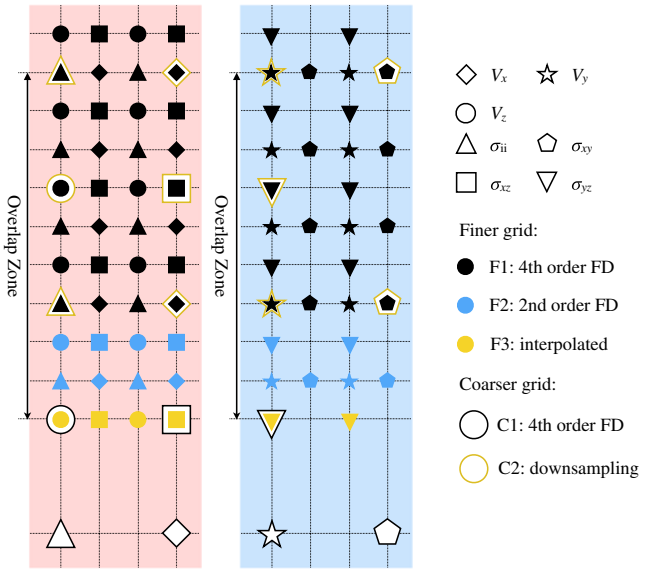

Figure 2. Distribution of velocity and stress components on *XZ* planes in the overlap zone between the fine and coarse meshes. The left and right planes correspond to the rear and front patches indicated in Figure 1. Filled and open symbols represent components in the fine and coarse grids area, respectively. In the overlap zone within fine mesh area, the filled circles F3 depict grid points where the wavefield is interpolated, filled circles F2 when the wavefield is updated by second-order FD, and filled circles F1 when the FD update is fourth-order accurate. In the overlap zone within the coarse mesh area, open circles C2 depict wavefield components downsampled from the fine grid components, and open circles C1 represent components updated by fourth-order FD. The color version of this figure is available only in the electronic edition.

grid need careful analysis. Regarding the first direction, some velocity and stress nodes adjacent to the grid interface in the upper fine layer cannot be updated by the fourth-order FD operators, due to missing grid points from the lower coarse region. To update the wavefield at these points, modified FD operators and other numerical methods are required. For example, Aoi and Fujiwara (1999) and Kristek *et al.* (2010) used interpolation and second-order FDs in slightly different implementations. Our approach is similar to that by Kristek *et al.* (2010), using interpolation and second-order FDs to update the wavefield at the missing coarse grid points (see Fig. 2).

To reproduce this method conveniently, we provide the order of calculations at every timestep as follows (see Fig. 2 for region labels).

Velocity field update:

1. fourth-order velocities update in the coarser region (C1),
2. fourth-order velocities update in the finer region (F1),
3. second-order velocities update in the finer region (F2),
4. free surface calculation,
5. interpolation of velocities in the finer region (F3), and
6. downsampling of velocities in the coarser region (C2).

Stress field update:

1. fourth-order stresses update in the coarser region (C1),
2. fourth-order stresses update in the finer region (F1),
3. second-order stresses update in the finer region (F2),
4. interpolation of stresses in the finer region (F3),
5. downsampling of stresses in the coarser region (C2), and
6. apply source.

To transmit the seismic waves from the fine to coarse grids, a downsampling scheme is needed. The most straightforward procedure (Kang and Baag, 2004b) is to simply insert the wavefield from the fine grid (filled symbols in Fig. 2) into the equivalent grid points in the coarse grids (open symbols). However, this method has proven unstable, due to the direct transfer of more high-frequency detailed signals present in the fine grid into the coarse grid with insufficient resolution to stably handle this information. Such instability often materializes after many timesteps in the wave propagation simulations. To stabilize the method, Hayashi *et al.* (2001) proposed using an averaging or weighting function on the wavefield information from the finer grids in the DM overlap zone, before transfer to the coarse grid. Kristek *et al.* (2010) and Zhang *et al.* (2013) filtered the velocities and stress tensors from the finer grids in the overlap zone by Lanczos (Duchon, 1979) and Gaussian downsampling schemes, respectively, before transferring the wavefield to the coarse grids. The necessity for interpolation is limited to a single horizontal plane in the overlap zone, and we choose the layer of the staggered grid that contains the least number of variables in need for interpolation (σ_{xz}, v_z, and σ_{yz}) to minimize the associated numerical error (similar to that used in Kristek *et al.*, 2010).

However, the proposed downsampling filters have not completely eliminated the stability issues for heterogeneous structure between the two grids (S. Aoi, written comm., 2016), in particular when a material interface crosses the boundary between the fine and coarse grids in other than a perpendicular direction (J. Kristek, written comm., 2016). We also note that Zhang *et al.* (2013) (3D collocated FD grid) and O. Rojas (unpublished report, see Data and Resources) both discovered that the Lanczos downsampling filter does not guarantee a stable simulation for their FD schemes. We introduce an alternative downsampling scheme, WEDMI, that gives stable solutions in a wide range of tests (though we found some exceptions that we discuss later) and may provide some computational advantages. Let the linear interpolation be expressed as

$$u = W \times U, \tag{2}$$

in which U is the field value on the coarse grid, u is the missing point on the fine grid, and W is the interpolation operator matrix. In previous studies, equation (2) is implemented by second-order (bilinear) (Kristek *et al.*, 2010) or third-order (trilinear) (Zhang *et al.*, 2013) matrices, which corresponds to 2D horizontal (the x–y plane) and 3D interpolation, respectively. Likewise, we have

$$U' = M \times u', \tag{3}$$

in which u' is the field value in the fine grid region, U' is located in the coarse grid, and M is the downsampling filter

(Kristek *et al.*, 2010; Zhang *et al.*, 2013). For WEDMI, we set $M = (h/H)W^T$, the normalized transpose of the interpolation operator matrix. Furthermore, in our scheme, we use bilinear interpolation to improve computational efficiency and allow for better scalability during future parallelization of the method. The matrix expression of bilinear interpolation is as follows:

$$u_{i,j} = \sum_I \sum_J W_{iI} U_{I,J} W^T_{Jj}, \tag{4}$$

in which (i, j) and (I, J) are the spatial indices on the 2D fine and coarse grids, respectively. In the case of 1D interpolation with $H/h = 3$, W can be described as

$$W = \begin{bmatrix} 1 & 0 & 0 & \cdots \\ 2/3 & 1/3 & 0 & \cdots \\ 1/3 & 2/3 & 0 & \cdots \\ 0 & 1 & 0 & \cdots \\ 0 & 2/3 & 1/3 & \cdots \\ 0 & 1/3 & 2/3 & \cdots \\ \vdots & \vdots & \vdots & \ddots \end{bmatrix}. \tag{5}$$

Correspondingly, we can extend WEDMI to 2D

$$U'_{I,J} = \left(\frac{h}{H}\right)^2 \sum_i \sum_j W^T_{Ii} u'_{i,j} W_{jJ}, \tag{6}$$

in which $u'_{i,j}$ depicts the value in the fine grid, $U'_{I,J}$ is located in the coarse grid, and the summation is applied on all wavefield terms in the fine grid indexed as (i, j). For $H/h = 3$ used here and using a 5×5-point-long filter, we get

$$U'_{I,J} = u'^{-}_{i,j} = \sum_{k=-2}^{2} \sum_{l=-2}^{2} \frac{1}{81}(3 - |k|)(3 - |l|) u'_{i+k,j+l}. \tag{7}$$

Equation (7) expresses an average of u at (i, j), using the surrounding 5×5 nodes (2D) with identical positions but different indices of $U'_{I,J}$ and $u'^{-}_{i,j}$. This approach has the property that the downsampling method from the fine to coarse grids is related to the interpolation from the coarse to fine grids by its matrix transpose operator. At the expense of losing this property, equation (7) can be generalized to a filter of $N \times N$ points as

$$U'_{I,J} = u'^{-}_{i,j} = \sum_{k=-\frac{N-1}{2}}^{\frac{N-1}{2}} \sum_{l=-\frac{N-1}{2}}^{\frac{N-1}{2}} \frac{1}{\left(\frac{(N+1)(N+3)}{4} - \frac{N+1}{2}\right)^2} \times \left(\frac{N+1}{2} - |k|\right)\left(\frac{N+1}{2} - |l|\right) u'_{i+k,j+l}, \tag{8}$$

in which N can be an arbitrary positive odd number. We note that, instead of using 13×13 fine-grid values as in the Lanczos and Gaussian filter implementations (with $H/h = 3$, Kristek *et al.*, 2010; Zhang *et al.*, 2013), bilinear interpolation as used in WEDMI can be formulated to use fewer points for downsampling. The lower number of points makes for a computationally more efficient method, easier to handle near the computational domain boundaries and less complicated for parallelization using Message Passing Interface. In the following four sections, we test WEDMI for accuracy and stability using different filter lengths. We also include the generalized equations for nth-order interpolation in m dimensions, as well as the corresponding downsampling filter in the Appendix.

The use of a DM requires additional scrutiny when using absorbing boundary condition (ABC) at the edges of the computational grid to limit artificial reflections. Here, we test WEDMI using ABCs or the sponge zones by Cerjan *et al.* (1985) implemented in AWP. Although the other types of ABCs have been shown to be more efficient, they can suffer from stability problems (e.g., some implementations of perfectly matched layers; see e.g., Festa *et al.*, 2005; Komatitsch and Martin, 2007), which may exacerbate numerical issues related to the DM. We align the sponge zones in the two grids using a physical width in the fine grid that is the same as that in the coarser grid.

Accuracy of AWP-DM with WEDMI

To verify the accuracy of AWP-DM with WEDMI (simplified as AWP-DM because all our tests have been done with the WEDMI method implemented), we use three scenarios: (1) a homogeneous half-space model with a point source, a subsection of the 3D Los Angeles (LA) basin model (SCEC CVM-S4) with both a point and an extended source (all the parameters of these scenarios are listed in Table 1). Our benchmarks of AWP-DM are compared to those by the original version of AWP using a uniform (fine) mesh, which has been thoroughly verified for both elastic and anelastic cases (Day *et al.*, 2001, 2003, 2005, 2008; Withers *et al.*, 2015). An explicit horizontal stress-free free surface boundary condition is applied at the top of the model (Gottschämmer and Olsen, 2001). For our following tests, we used WEDMI with a 5-point downsampling filter, because the difference in accuracy between the different filter lengths is negligible (see Ⓔ Fig. S2, available in the electronic supplement to this article).

A Homogeneous Half-Space Model with a Point Source

We first test AWP-DM in a homogeneous half-space model (parameters are listed in the Homogeneous Model column in Table 1). We place the grid interface at a depth of 11,250 m, above which the spatial grid size (h) is 75 m, and below which we use 225 m (H). The P-wave velocity, S-wave velocity, and density are 2500 m/s, 1500 m/s, and 2300 kg/m^3, respectively. For both the fine- and coarse-grid regions, we sample the S wavelength by at least five nodes. The sponge zones are 20 and 60 grid points thick in the coarse and fine grids, respectively. The point source is centered in the model, 18,000 m below the free surface. We apply a double-couple source with strike 0°, dip 90°, and rake

Table 1
Parameters of Models

	Dimension X (m), Y (m), Z (m)	Depth of Overlap Zone (m)	Source Location X (m), Y (m), Z (m)*	Grid Spacing H (m), h (m)	Time Interval dt (s)	Thickness of Absorbing Boundary (m)	Timesteps
Homogeneous model	38,250, 38,250, 29,250	11,250	19,125, 19,125, 11,250	225, 75	0.014	4500	3000
3D LA model-1	38,250, 38,250, 29,250	11,250	19,125, 19,125, 11,250	225, 75	0.005	4500	6000
3D LA model-2	22,500, 22,500, 20,050	3825	15,000–17,250, 11,250, 15,075–17,325	225, 75	0.005	2250	10,000
3D LA model-3	67,500, 67,500, 42,525	4275	33,750, 33,750, 33,750	225, 75	0.005	6750	280,000
3D LA model-4	45,000, 45,000, 42,525	4275	22,500, 22,500, 33,750	225, 75	0.005	6750	800,000
Large contrast basin model	22,500, 22,500, 20,050	3825	11,250, 11,250, 11,250	225, 75	0.005	2250	1,000,000

LA, Los Angeles.
*Z (m) is measured from the model bottom.

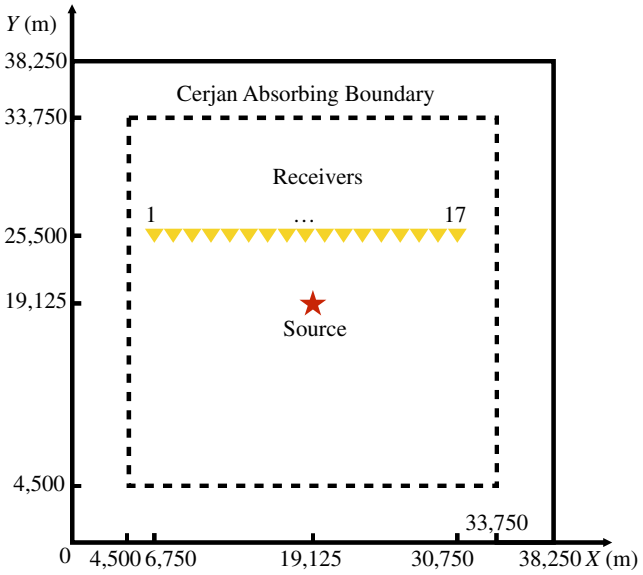

Figure 3. Surface (XY) slice of the homogeneous half-space model depicting model dimensions and point-source location. The model size, source location, and width of sponge zones are described in the Homogeneous Model column in Table 1. The receivers (triangles) on the free surface are aligned along the X direction ($y = 25,500$ m) from $x = 6750$ m to $x = 30,750$ m, with a spacing of 1500 m. The color version of this figure is available only in the electronic edition.

180° (right-lateral strike-slip mechanism), using a Gaussian wavelet with a maximum frequency of 1 Hz.

We compare the ground motion at 17 receivers spaced 1500 m apart and aligned along the x direction on the free surface (see Fig. 3) from AWP-DM to that obtained from AWP with uniform (fine) spatial discretization (h). The two solutions are nearly identical to the naked eye in both phase and amplitude, including a close-up of the fifth station (Fig. 4), with an average cross-correlation coefficient between simulated waveforms from AWP-DM and the uniform fine grid over all stations of 99.2%.

3D SCEC CVM (Los Angeles Basin) with Point and Extended Fault Sources

Here, we apply our DM scheme to a much more complex model, namely a subsection of the SCEC CVM-S4 (Magistrale *et al.*, 2000; Kohler *et al.*, 2003) including the LA basin, as shown in Figure 5 and the parameters listed in the 3D LA Model-1 column in Table 1. The LA basin is a sediment-filled and complex-shaped structure with a large variation in seismic velocities between shallow sediments and deep crystalline-basement rock. More than 10 million people live in the greater LA area where a modern metropolitan infrastructure leads to a high risk in a region with large seismic hazards. For our tests, we limit the minimum V_S to 400 m/s in the near surface, although lower values are present in the CVM. The largest V_S in the model is 4500 m/s.

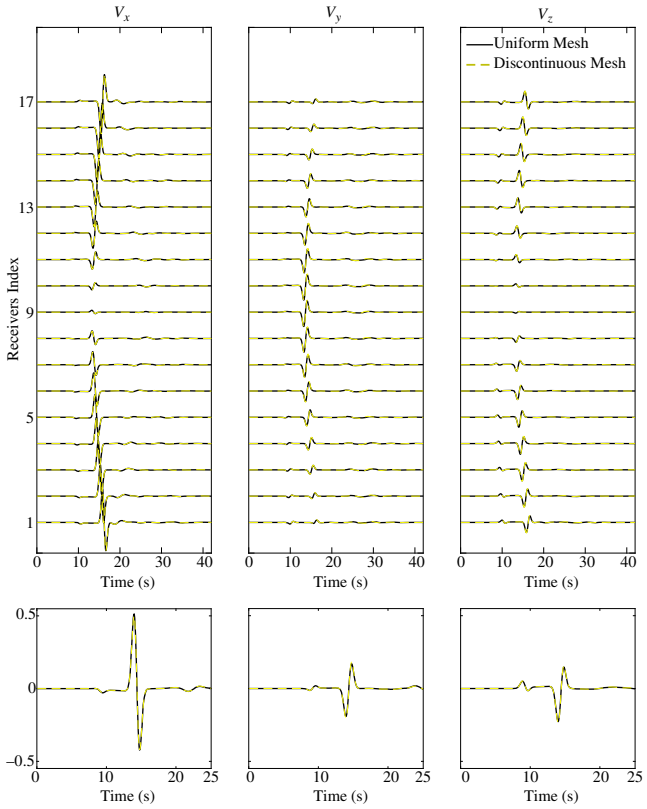

Figure 4. Comparison of waveforms obtained from DM (dashed traces) and uniform fine mesh (solid traces) simulations for the homogeneous half-space model (the Homogeneous Model column in Table 1; Fig. 3). Receiver indices are described in Figure 3 (left) V_x, (middle) V_y, and (right) V_z. Upper panel shows all 17 stations' waveforms; bottom panel shows detailed waveform comparison for Station 5. The color version of this figure is available only in the electronic edition.

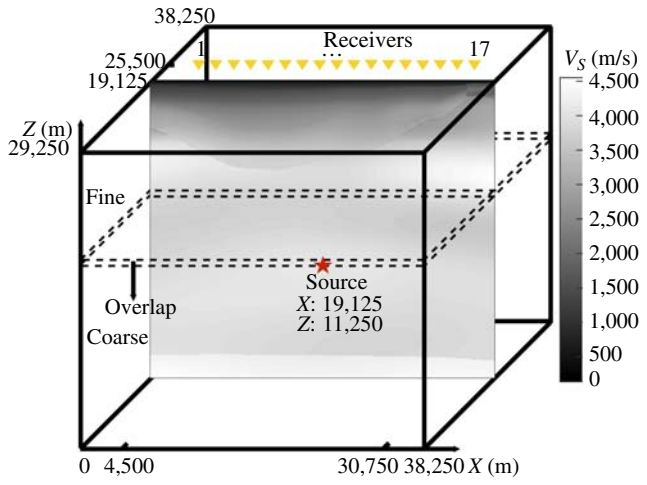

Figure 5. V_S along the XZ plane from extraction of the 3D Southern California Earthquake Center (SCEC) Community Velocity Model (CVM) S4, including the Los Angeles (LA) basin (3D LA model-1). The star depicts the location of our point source. V_S ranges from 400 to 4500 m/s. The color version of this figure is available only in the electronic edition.

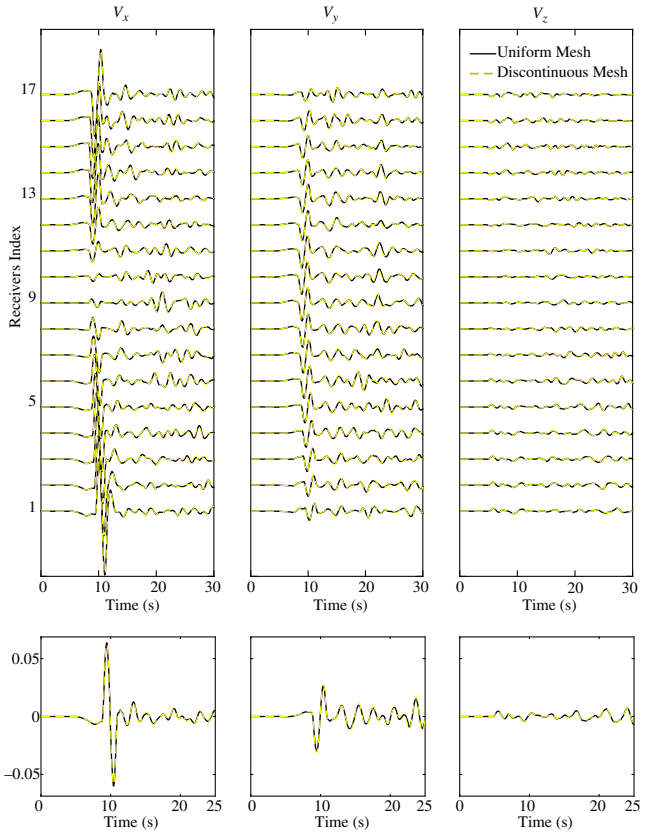

Figure 6. Comparison of waveforms obtained from DM (dashed traces) and uniform fine (solid traces) mesh simulations for the 3D LA basin model with a point source (see the 3D LA Model-1 column in Table 1 and Fig. 5 for model geometry). Upper panel shows all 17 stations' waveforms; bottom panel shows detailed waveform comparison for Station 5. The color version of this figure is available only in the electronic edition.

For our first test, we apply the same model size, depth of grid interface, grid spacing, point-source location and mechanism, and location of receivers as used for the homogeneous half-space described above (Fig. 5). We use a Hann wavelet with a maximum frequency of 1 Hz. The signal durations are extended compared to those for the homogeneous model, due to 3D basin and other heterogeneity effects generating reflections and scattering. The solution from the DM is satisfactorily close to the uniform mesh solution (the average cross-correlation coefficient between waveforms from AWP-DM and the uniform fine grid is 98.7%) even in the zoomed-in time window (Fig. 6), with small discrepancies at some receivers, likely caused by a combination of the coarser discretization of the deeper layers, as well as approximations in the grid overlap region by AWP-DM.

We also apply a benchmark in the 3D LA basin model that consists of a finite-fault source that crosses the overlap zone between fine and coarse regions. This scenario has a more complex fault model and may be more suitable as an indicator of numerical accuracy than the previous two models. Figure 7 and Table 1 show the model setup (the 3D LA

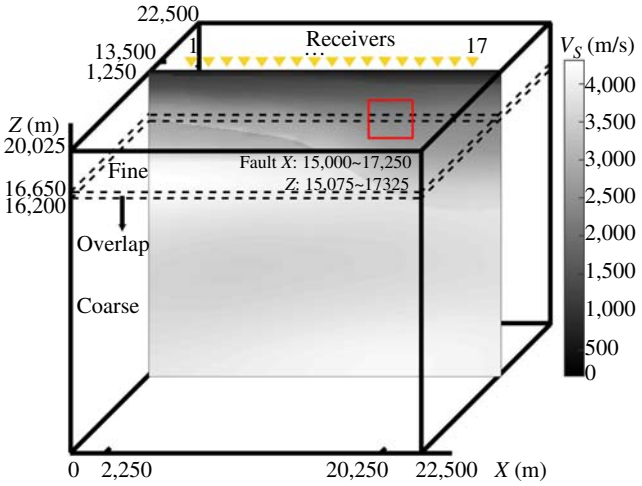

Figure 7. V_S along XZ plane from extraction of the 3D SCEC CVM-S4 including the LA basin. The model parameters are described in the 3D LA Model-2 column in Table 1. V_S ranges from 500 to 4500 m/s. The 17 receivers (triangles) at free surface are located at $y = 11{,}250$ m from $x = 2250$ m to $x = 20{,}250$ m, deployed every 1125 m. The square patch on the fault depicts the extent of the source. The color version of this figure is available only in the electronic edition.

Model-2 column in Table 1, 24 million grid points for a uniform mesh with a grid spacing of 75 m). The DM interface is located at a depth of 3825 m, and the intersecting rectangular fault has dimensions of 2250 m (x) × 2250 m (z), consisting of 900 subfaults. Figure 8a shows snapshots of the σ_{xz} moment-rate component on fault, in which the kinematic source is initiated at the center and propagates radially to the edges with a constant rupture velocity of 3000 m/s. Figure 8b,c shows the normalized source time function in the time and frequency domains for all the subfaults. Figure 9 compares the waveforms at the 17 sites (see Fig. 7) for discontinuous and uniform mesh solutions. Despite the higher complexity in the wavefields generated by the finite-source and 3D structural model, the difference between the fine uniform grid and DM solutions are visually negligible (average cross-correlation coefficient of 98.3%). In summary, our three verification tests, a homogeneous half-space, and 3D LA basin model with point and extended sources, all demonstrate great accuracy of our AWP-DM.

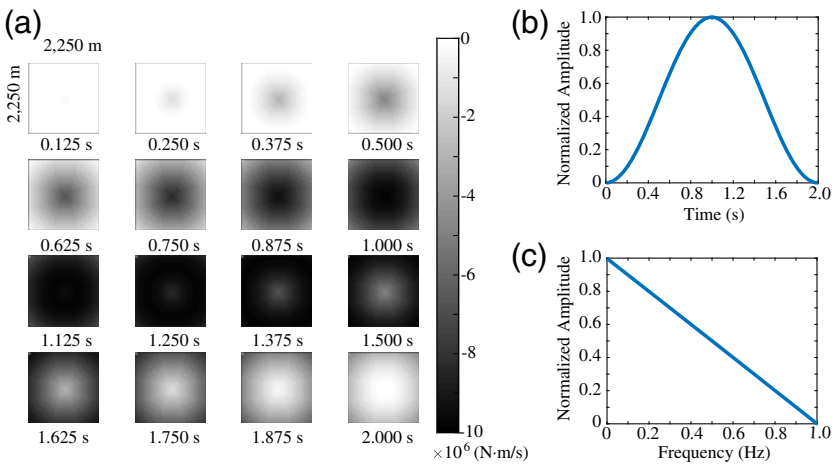

Figure 8. (a) Snapshots of the rupture propagation (σ_{xz} component of the moment rate) from 0.125 to 2.000 s. Fault dimensions are listed in Table 1. (b) Normalized source time function in the time domain. (c) Normalized source time function in the frequency domain. The color version of this figure is available only in the electronic edition.

Stability Analysis of AWP-DM

As discussed above, stability appears to be a pervasive problem for discontinuous staggered-grid mesh configurations for highly complex media. In this section, we explore the stability conditions for AWP-DM with significantly extended simulation time (from 270,000 to 1,000,000 timesteps, depending on platform limits) in models of varying complexity and using different downsampling filter lengths. First, we use the 3D LA basin model (the 3D LA Model-3 column in Table 1), with the source located at the center of the model and 8775 m below the free surface. The DM interface is located at a depth of 4275 m, resulting in the depth of 19 grid points for coarse grids. Figure 10 compares solutions from AWP-DM with the WEDMI downsampling (5-point filter) and to the solution with no filter (directly inserting the wavefield from the fine grid into the equivalent grid points in the coarse grid). The solution without a downsampling filter shows instability starting at about 670 s (134,000 steps), in agreement with the results by Zhang *et al.* (2013). In comparison, our solution using the WEDMI technique shows stable results up to 1400s (280,000 steps), a range that exceeds current large-scale simulation models. The length of the simulation was constrained by computational limitation and not by issues related to stability.

We use a slightly smaller subset from the 3D LA basin model (see the 3D LA Basin-4 column in Table 1) to extend the simulation time, with the same vertical location of the DM interface as for the larger 3D model. Similarly, the source is located in the center of the model, with the same vertical distance below the DM grid interface as for the large 3D model. Figure 11 (note the logarithmic axes) shows that our AWP-DM using WEDMI is stable up to 800,000 timesteps, beyond the length required by most current and expected near-future high-frequency ground-motion simulations. Again, the maximum number of timesteps was dictated by computational resources only.

To examine the influence of the frequency content of the source on the stability of AWP-DM (downsampling filter length of 5), we use a temporal delta function with the 3D LA model-3. Ⓔ Figure S1a shows that this model is stable

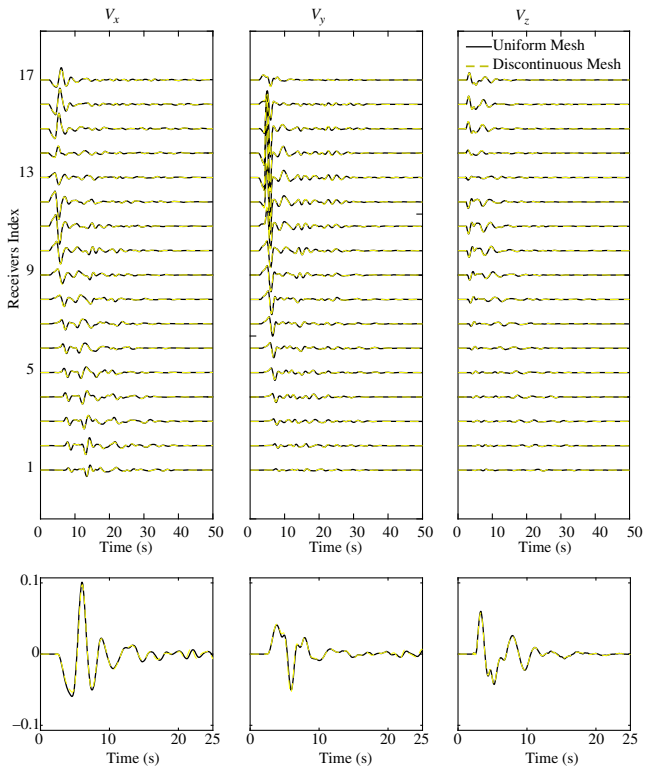

Figure 9. Comparison of waveforms obtained from DM (dashed traces) and uniform fine mesh (solid traces) simulations for the 3D LA basin model with a finite fault (see Figs. 7 and 8; the 3D LA Model-2 column in Table 1). Upper panel shows all 17 stations' waveforms; bottom panel shows detailed waveform comparison for Station 17. The color version of this figure is available only in the electronic edition.

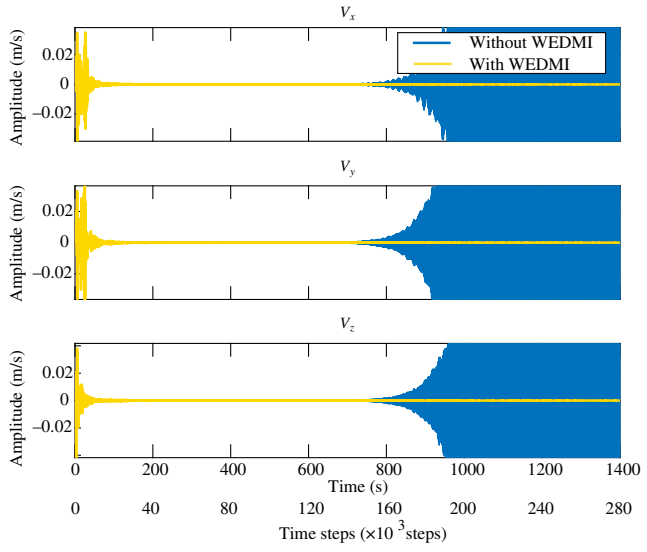

Figure 10. Comparison of simulation results from DM simulations using wavefield estimation using a discontinuous mesh interface (WEDMI) and simply inserting the wavefield from the fine grids into the coarse grid (no downsampling filter). The results are generated in the 3D LA Model-3 column in Table 1. The color version of this figure is available only in the electronic edition.

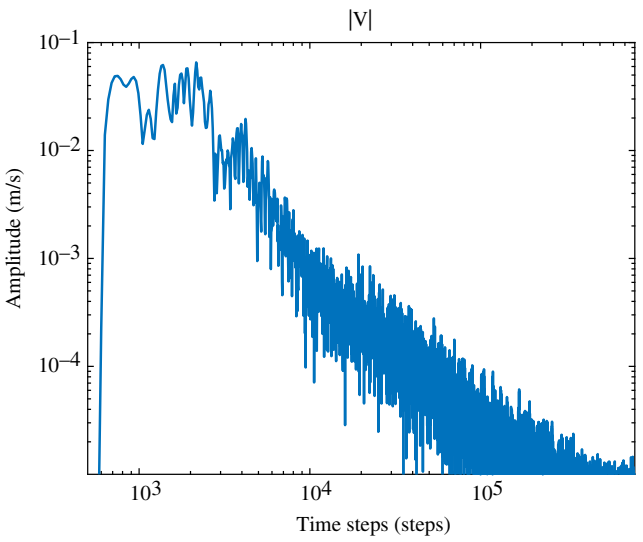

Figure 11. Stability test of WEDMI DM scheme using the 3D LA Model-4 column in Table 1. We plot $\log_{10}$ of velocity magnitude to emphasize the bounded energy over 0.8 million timesteps. The color version of this figure is available only in the electronic edition.

to at least 270,000 timesteps, for which the run time was dictated by computational resources. An additional test with a smaller domain size (same domain size with 3D LA model-2) was stable up to 1 million timesteps (Ⓔ Fig. S1b). These tests imply that the stability of AWP-DM with WEDMI is insensitive to the frequency content of the seismic source.

Finally, we challenge the AWP-DM method with an extreme test case: a strong-contrast basin model (Fig. 12 and the Large Contrast Basin Model column in Table 1), which has low-velocity sediments (V_P 1500 m/s, V_S 500 m/s, and density 1900 kg/m^3) located above higher-velocity bedrock (V_P 2500 m/s, V_S 1500 m/s, and density 2300 kg/m^3). The presence of the abrupt (factor of 3) contrast of V_S along x, y,

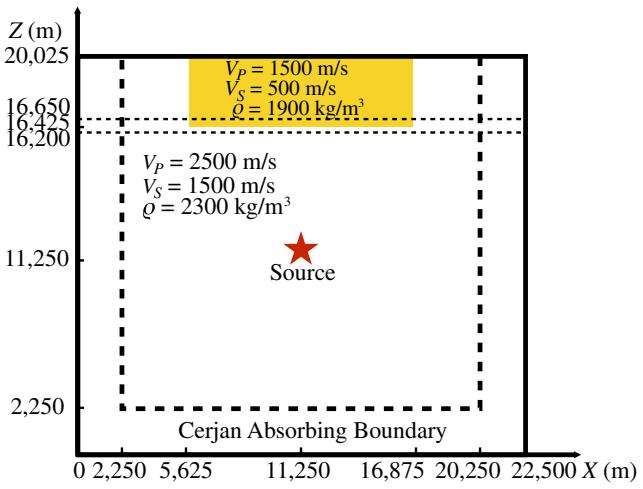

Figure 12. Description of our large-contrast basin model used for our stability test. The color version of this figure is available only in the electronic edition.

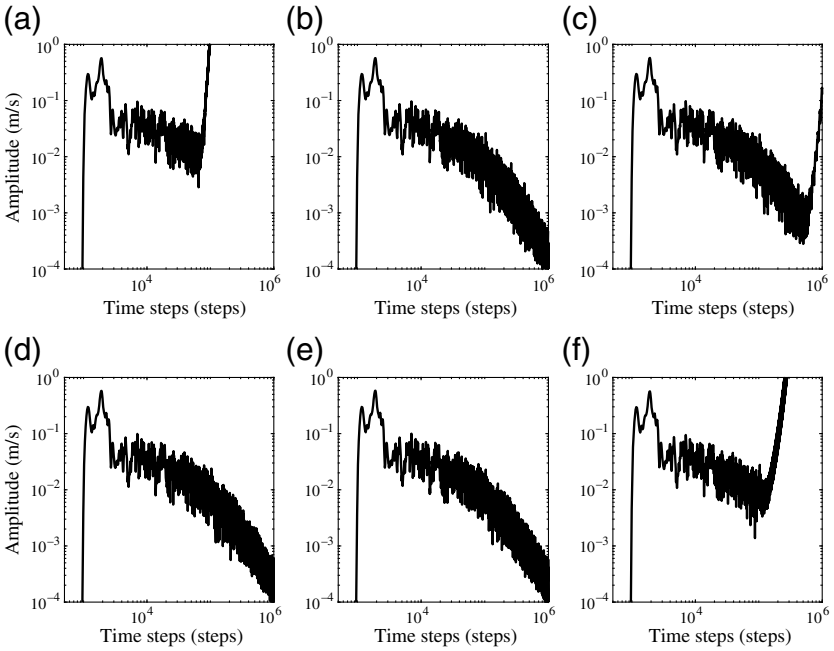

Figure 13. Stability test of our large-contrast basin model using WEDMI with different filter lengths: (a) 5 points, (b) 7 points, (c) 9 points, (d) 11 points, (e) 13 points, and (f) Lanczos 13p.

and z directions inside the DM overlap zone can be considered an extreme indicator of stability because this model can trap much more slowly decaying energy, compared to the homogeneous and realistic 3D LA basin models. We tested the extreme model using WEDMI with downsampling filter lengths of 5, 7, 9, 11, and 13 points, as well as using the Lanczos filter (filter length of 13, Lanczos 13p) (Ⓔ Fig. S2 and Fig. 13), at a receiver located at (9000 m, 9000 m) on the surface. In this test, different downsampling filter implementations show comparable accuracy (Ⓔ Fig. S2) but different stability results: WEDMI is stable to at least 1,000,000 timesteps, with downsampling filter lengths of 7, 11, and 13 but only to ~70,000 and ~750,000 for downsampling filter lengths of 5 and 9 points, respectively. In comparison, Lanczos 13p is stable to ~160,000 timesteps for the extreme model. Another extreme scenario, with a dipping basin bottom boundary intersecting the DM overlap zone demonstrated in Ⓔ Figure S3a, is tested as a further test of stability. WEDMI with filter lengths of 7, 9, 11, and 13 remains stable to at least 1,000,000 timesteps, whereas WEDMI with filter length of 5 and Lanczos 13p are stable until around 700,000 timesteps. These tests imply that instability is possible in models with large velocity contrasts inside the DM overlap zone. In summary, our benchmarks indicate that AWP-DM is accurate and stable for models in which the transitional mesh region is disjointed from very strong velocity interfaces and otherwise can be stabilized by extending the downsampling filter length.

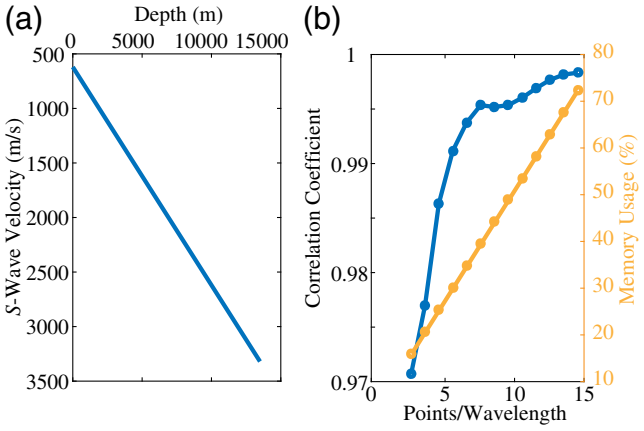

Figure 14. (a) S-wave velocity of 1D model used to explore trade-off between depth of the overlap zone and accuracy. The P-wave velocity is 1.7 times the S-wave velocity, and the density is 2000 kg/m^3. (b) Cross-correlation coefficient of the first 30 s of synthetics computed from DM and uniform (fine) mesh methods as a function of the number of points per S wavelength (points per wavelength [ppw]). The memory usage (100 × the ratio between the memory used by AWP-DM and the uniform fine FD methods) as a function of ppw is also shown. The color version of this figure is available only in the electronic edition.

Discussion

The primary incentive to develop a stable and accurate DM FD method is to save computational resources, compared to the requirements for a uniform mesh code. We expect a trade-off between the accuracy and computational cost by means of adjusting the depth of the DM interface. The shallower we can position the DM interface, the smaller the region that needs to be discretized by the fine grid, with a larger computational saving as result. On the other hand, a shallow location of the DM interface may cause insufficient sampling of the wavefield in the lower velocity material and cause inaccurate results. To capture this trade-off, we perform a test with the 1D model shown in Figure 14a, in which the source is located at a depth of 16,650 m below free surface. The receiver is located 3181 m northeast of the source on the surface. We correlate the simulated waveforms from AWP-DM and uniform (fine) grid AWP for a range of depths of the DM grid interface. Figure 14b shows the cross-correlation coefficient of the first 30 s of waveforms from uniform and discontinuous meshes, plotted against the number of points per S wavelength in the coarse grid (points per wavelength [ppw]) associated with the depth of the DM grid interface. This figure suggests an optimal depth of the DM interface corresponding to 7–8 ppw calculated from the coarse grid in the overlap zone (with a correlation coefficient

of ∼0.995), with smaller gains in accuracy at deeper locations. We note that the increase of the usual rule of thumb for a fourth-order staggered-grid scheme of at least 5 ppw is only required inside the DM overlap zone and is therefore not computationally significant. Figure 14b also shows that the depth of the interface associated with 7–8 ppw corresponds to the use of about 40% of memory for the corresponding (fine) uniform grid. In general, the figure can be used to decide on the positioning of the DM interface dependent on model-specific requirements for accuracy and available computational resources.

Conclusions

We implemented a DM scheme for the fourth-order accurate staggered-grid velocity-stress AWP FD method, with a ratio of the coarse-to-fine grid spacing of 3. Our method applies bilinear interpolation and second-order FD to update the wavefield at the grid points of the fine mesh undefined in the coarse grid and a novel approach to downsample variables from the fine grid to the coarse grid (WEDMI). We show that our AWP-DM scheme is accurate and stable for a number of timesteps, exceeding current ground-motion simulation requirements for a homogeneous model and a 3D LA basin velocity model using a point and extended source intersecting the interface between the fine and coarse meshes. For extreme models, for example, with a factor of 3 *S*-wave velocity contrast located inside the DM overlap zone, the WEDMI downsampling filter length should be chosen with care, because some cases (e.g., 5- and 9-point filters) appear to be less stable than others. In any case, WEDMI has the potential to significantly improve the efficiency of current (uniform mesh) FD methods, especially for simulations with realistic 3D geological settings and near-surface low velocities. Implementation of WEDMI is expected to be straightforward for other FD or finite-element schemes.

Data and Resources

The Southern California Earthquake Center (SCEC) Community Velocity Model (CVM) S4 can be downloaded from http://scec.usc.edu/scecpedia/ (last accessed November 2016). Most data processing and visualization were done by MATLAB (http://www.mathworks.com/products/matlab/, last accessed November 2016). We cite an unpublished report about the instability of a discontinuous mesh mimetic operator finite-difference method from Otilio Rojas in 2014. He analyzes instability of his discontinuous mesh method and found that the multiple choices of interpolations and downsampling filters perform differently.

Acknowledgments

We would like to thank Jozef Kristek and one other anonymous reviewer for their suggestions, leading to an improved article. This research was supported by Southern California Earthquake Center (SCEC) Contribution Number 7911 and by National Science Foundation (NSF) Award ACI-1450451. SCEC is funded by NSF Cooperative Agreement EAR-1033462 and U.S. Geological Survey (USGS) Cooperative Agreement G12AC20038.

References

Aoi, S., and H. Fujiwara (1999). 3D finite-difference method using discontinuous grids, *Bull. Seismol. Soc. Am.* **89,** 918–930.

Cerjan, C., D. Kosloff, R. Kosloff, and M. Reshef (1985). A nonreflecting boundary condition for discrete acoustic and elastic wave equations, *Geophysics* **50,** 705–708.

Cui, Y., K. B. Olsen, T. H. Jordan, K. Lee, J. Zhou, P. Small, D. Roten, G. Ely, D. K. Panda, A. Chourasia, *et al.* (2010). Scalable earthquake simulation on petascale supercomputers, *2010 ACM/IEEE International Conf. for High Performance Computing, Networking, Storage and Analysis*, 20 pp., doi: 10.1109/sc.2010.45.

Cui, Y., E. Poyraz, K. B. Olsen, J. Zhou, K. Withers, S. Callaghan, J. Larkin, C. Guest, D. Choi, A. Chourasia, *et al.* (2013). Physics-based seismic hazard analysis on petascale heterogeneous supercomputers, *Proc. of the International Conf. on High Performance Computing, Networking, Storage and Analysis*, ACM, Denver, Colorado, 1–12, doi: 10.1145/2503210.2503300.

Day, S., J. Bielak, D. Dreger, R. Graves, S. Larsen, K. Olsen, and A. Pitarka (2001). *Tests of 3D Elastodynamic Codes: Final Report for Lifelines Project 1A01*, Pacific Earthquake Engineering Research Center.

Day, S., J. Bielak, D. Dreger, R. Graves, S. Larsen, K. Olsen, and A. Pitarka (2003). *Tests of 3D Elastodynamic Codes: Final Report for Lifelines Project 1A02*, Pacific Earthquake Engineering Research Center.

Day, S., J. Bielak, D. Dreger, R. Graves, S. Larsen, K. Olsen, and A. Pitarka (2005). *Tests of 3D Elastodynamic Codes: Final Report for Lifelines Project 1A03*, Pacific Earthquake Engineering Research Center.

Day, S. M., R. Graves, J. Bielak, D. Dreger, S. Larsen, K. B. Olsen, A. Pitarka, and L. Ramirez-Guzman (2008). Model for basin effects on long-period response spectra in southern California, *Earthq. Spectra* **24,** 257–277.

Duchon, C. E. (1979). Lanczos filtering in one and two dimensions, *J. Appl. Meteorol.* **18,** 1016–1022.

Festa, G., E. Delavaud, and J. P. Vilotte (2005). Interaction between surface waves and absorbing boundaries for wave propagation in geological basins: 2D numerical simulations, *Geophys. Res. Lett.* **32,** L20306, doi: 10.1029/2005GL024091.

Gottschämmer, E., and K. B. Olsen (2001). Accuracy of the explicit planar free-surface boundary condition implemented in a fourth-order staggered-grid velocity-stress finite-difference scheme, *Bull. Seismol. Soc. Am.* **91,** 617–623.

Hayashi, K., D. R. Burns, and M. N. Toksoz (2001). Discontinuous-grid finite-difference seismic modeling including surface topography, *Bull. Seismol. Soc. Am.* **91,** 1750–1764.

Jastram, C., and A. Behle (1992). Acoustic modeling on a grid of vertically varying spacing, *Geophys. Prospect.* **40,** 157–169.

Kang, T. S., and C. E. Baag (2004a). An efficient finite-difference method for simulating 3D seismic response of localized basin structures, *Bull. Seismol. Soc. Am.* **94,** 1690–1705.

Kang, T. S., and C. E. Baag (2004b). Finite-difference seismic simulation combining discontinuous grids with locally variable timesteps, *Bull. Seismol. Soc. Am.* **94,** 207–219.

Kohler, M. D., H. Magistrale, and R. W. Clayton (2003). Mantle heterogeneities and the SCEC reference three-dimensional seismic velocity model version 3, *Bull. Seismol. Soc. Am.* **93,** 757–774.

Komatitsch, D., and R. Martin (2007). An unsplit convolutional perfectly matched layer improved at grazing incidence for the seismic wave equation, *Geophysics* **72,** Sm155–Sm167.

Kristek, J., P. Moczo, and M. Galis (2010). Stable discontinuous staggered grid in the finite-difference modelling of seismic motion, *Geophys. J. Int.* **183,** 1401–1407.

Magistrale, H., S. Day, R. W. Clayton, and R. Graves (2000). The SCEC southern California reference three-dimensional seismic velocity model version 2, *Bull. Seismol. Soc. Am.* **90,** S65–S76.

Moczo, P. (1989). Finite-difference technique for SH-waves in 2-D media using irregular grids applications to the seismic response problem, *Geophys. J. Int.* **99,** 321–329.

Olsen, K. B. (1994). *Simulation of Three Dimensional Wave Propagation in the Salt Lake Basin*, University of Utah, Salt Lake City, Utah.

Olsen, K. B., R. J. Archuleta, and J. R. Matarese (1995). Three-dimensional simulation of a magnitude 7.75 earthquake on the San Andreas fault, *Science* **270,** 1628–1632.

Olsen, K. B., S. M. Day, L. A. Dalguer, J. Mayhew, Y. Cui, J. Zhu, V. M. Cruz-Atienza, D. Roten, P. Maechling, T. H. Jordan, *et al.* (2009). ShakeOut-D: Ground motion estimates using an ensemble of large earthquakes on the southern San Andreas fault with spontaneous rupture propagation, *Geophys. Res. Lett* **36,** L04303, doi: 10.1029/2008GL036832.

Olsen, K. B., S. M. Day, J. B. Minster, Y. Cui, A. Chourasia, M. Faerman, R. Moore, P. Maechling, and T. Jordan (2006). Strong shaking in Los Angeles expected from southern San Andreas earthquake, *Geophys. Res. Lett* **33,** L07305, doi: 10.1029/2005GL025472.

Olsen, K. B., S. M. Day, J. B. Minster, Y. Cui, A. Chourasia, D. Okaya, P. Maechling, and T. Jordan (2008). TeraShake2: Spontaneous rupture simulations of M_w 7.7 earthquakes on the southern San Andreas fault, *Bull. Seismol. Soc. Am.* **98,** 1162–1185.

Pitarka, A. (1999). 3D elastic finite-difference modeling of seismic motion using staggered grids with nonuniform spacing, *Bull. Seismol. Soc. Am.* **89,** 54–68.

Tessmer, E. (2000). Seismic finite-difference modeling with spatially varying time steps, *Geophysics* **65,** 1290–1293.

Wang, Y., J. Xu, and G. T. Schuster (2001). Viscoelastic wave simulation in basins by a variable-grid finite-difference method, *Bull. Seismol. Soc. Am.* **91,** 1741–1749.

Withers, K. B., K. B. Olsen, and S. M. Day (2015). Memory-efficient simulation of frequency-dependent Q, *Bull. Seismol. Soc. Am.* **105,** 3129–3142.

Zhang, Z. G., W. Zhang, H. Li, and X. F. Chen (2013). Stable discontinuous grid implementation for collocated-grid finite-difference seismic wave modelling, *Geophys. J. Int.* **192,** 1179–1188.

Appendix

Here we provide the generalized equations for our proposed interpolation and corresponding downsampling methods. The 1D nth-order interpolation can be expressed as

$$f(x) = \sum_{i=1}^{n} a(x_i) f(x_i) = A_{1\times n} \times F_{n\times 1}, \tag{A1}$$

in which $f(x)$ is the function to be interpolated positioned at x, and $f(x_i)$ and $a(x_i)$ are the known nodal values of the function and weight coefficient at each value of x_i. The interpolated function is the summation of all the products of weight coefficients and nodal values over the n points. The weight coefficient at x_i is also dependent on the relative distance between x and x_i. The rightmost side of equation (A1) expresses the interpolation in matrix format.

Next, we extend this to m-dimensional nth-order interpolation; the equation can be formulated as

$$\begin{aligned} f(\vec{x}) &= \sum_{i_1=1}^{n}\sum_{i_2=1}^{n}\cdots\sum_{i_m=1}^{n} a(x_{i_1,i_2,\cdots i_m}) f(x_{i_1,i_2,\cdots i_m}) \\ &= \sum_{i_1=1}^{n}\sum_{i_2=1}^{n}\cdots\sum_{i_m=1}^{n}\prod_{j=1}^{m} a(x_j) f(x_{i_1,i_2,\cdots i_m}), \end{aligned} \tag{A2}$$

in which $\vec{x}$ is an arbitrary position in an m-dimensional Hilbert space, and $i_1 \ldots i_m$ correspond to each point in one of the dimensions. The matrix expression of interpolating n_2 points (1 point assumed in equations A1 and A2) out of n_1 points in each dimension is

$$\begin{aligned} f_{n_2^m} &= A_{n_2\times n_1} \times F_{n_1^m} \times (A_{n_1\times n_2} : A_{n_1\times n_2} : \ldots : A_{n_1\times n_2}) \\ &= A_{n_2\times n_1} F_{n_1^m} B_{n_1^{(m-1)}\times n_2^{(m-1)}}, \end{aligned} \tag{A3}$$

in which the subscript of each term describes the dimension of the matrix. For example, $f_{n_2^m}$ is a matrix in which the dimension is $n_2 \times n_2 \cdots \times n_2$ (m multipliers in total).

Similarly, the matrix form of downsampling into n_1 points from n_2 points is

$$F_{n_1^m} = \left(\frac{n_1}{n_2}\right)^m (A_{n_2\times n_1})^T f_{n_2^m} (B_{n_1^{(m-1)}\times n_2^{(m-1)}})^T. \tag{A4}$$

In both the interpolation and downsampling equations (A3) and (A4), $F_{n_1^m}$ and $f_{n_2^m}$ denote field values in the coarser and finer grids, respectively.

Department of Geological Sciences
San Diego State University
5500 Campanile Drive
San Diego, California 92182
snie-w@sdsu.edu
yow004@ucsd.edu
kbolsen@mail.sdsu.edu
sday@mail.sdsu.edu
(S.N., Y.W., K.B.O., S.M.D.)

Manuscript received 9 March 2017;
Published Online 25 September 2017